Open Access

Catalysis Research

LIDSEN Publishing Inc.

Research Article

3D Fe_3O_4-decorated Nitrogen-doped Graphene Aerogel as a Highly Durable Electrocatalyst for Oxygen Reduction Reactions

Jia Yu, Haiyan Jing, Zongdeng Wu, Boyuan Liu, Wu Lei *, Qingli Hao *

School of Chemistry and Chemical Engineering, Nanjing University of Science and Technology, Nanjing 210094, China; E-Mails: yujia@njust.edu.cn; Jhy24@njust.edu.cn; zongdengwu@njust.edu.cn; liuboyuan@njust.edu.cn; leiwuhao@njust.edu.cn; qinglihao@njust.edu.cn

* **Correspondence:** Wu Lei and Qingli Hao; E-Mails: leiwuhao@njust.edu.cn; qinglihao@njust.edu.cn

Academic Editor: Shijun Liao

Special Issue: Electrocatalysis in Fuel Cells

Catalysis Research
2022, volume 2, issue 2
doi:10.21926/cr.2202016

Received: April 29, 2022
Accepted: June 08, 2022
Published: June 21, 2022

Abstract

The rational design of efficient electrocatalysts for oxygen reduction reaction (ORR) is the key to developing fuel cells and metal-air batteries. Carbon-supported iron-based materials, as the most promising electrocatalysts for ORR, have drawn much attention as they are cost-effective and exhibit high activity. In this work, a three-dimensional (3D) Fe_3O_4-decorated N-doped graphene aerogel (Fe_3O_4/NGA) catalyst was synthesized following a simple hydrothermal method which was followed by an annealing process. The complex formed between Fe^{2+} and phenanthroline was first used as the precursor of iron and nitrogen sources to synthesize Fe_3O_4 nanocrystals. Benefiting from the synergistic effect between the uniformly distributed Fe_3O_4 nanoparticles and the 3D porous N-doped graphene aerogel, Fe_3O_4/NGA exhibits good electrocatalytic activity with a half-wave potential of 0.81 V. It also exhibits excellent selectivity with low HO_2^- yield (<5%), and excellent long-time stability. The encouraging results demonstrate that the Fe_3O_4/NGA composite catalyst is a promising candidate that can be used for the fabrication of non-precious electrocatalyst for ORR.

Keywords
Oxygen reduction reaction; Fe_3O_4 nanoparticles; N-doped graphene aerogel; electrocatalyst

1. Introduction

Proton exchange membrane fuel cells (PEMFCs) and metal-air batteries, as efficient energy conversion devices, have been widely studied in recent decades; however, the sluggish kinetics characterizing the cathodic oxygen reduction reaction (ORR) restricts the development of these systems [1, 2]. ORR is a complicated multielectron transfer process with various reaction pathways ($2e^-$ and $4e^-$). Therefore, the rational design of electrocatalysts is the key to achieving superior activity, high selectivity, and excellent durability [3]. Platinum-based catalysts exhibit excellent catalytic activity towards $4e^-$ ORR, but the high cost, poor stability, and methanol resistance of such catalysts make it necessary to explore alternative candidates [4].

Transition metal compounds such as oxides [5-7], nitrides [8, 9], carbides [10], etc., have been widely studied as efficient electrocatalysts. Fe-based compounds have been widely explored catalysts. Fe is one of the earth-abundant transition metals. Fe_3O_4, an oxide of Fe, is characterized by good electrical conductivity (>100 S cm^{-1}), high specific surface area, and chemical stability in an alkaline medium [11-13]. Nanostructured Fe_3O_4 species are considered one of the most promising catalysts for ORR as they exhibit outstanding electrolytic activity [14, 15]. However, a series of problems (such as the dissolution or corrosion) is encountered if pure Fe_3O_4 nanoparticles are directly used as catalysts. Nanostructured Fe_3O_4 species can be combined with carbon materials to form composite catalysts to effectively address these problems [16]. Especially, the nitrogen-doped carbon materials [17, 18] are excellent candidates as the pyridinic-N and Fe-N-C have been reported to be the active sites for ORR [19, 20]. Among these carbon materials, graphene has attracted immense attention as it exhibits good conductivity, thermal stability, and chemical stability and is characterized by a large surface area [21, 22]. Graphene oxide (GO), a common precursor for the preparation of graphene, contains a large number of oxygen-containing groups on the surfaces and edges. These groups can provide an abundant number of sites to attach with the metal species that are used as precursors. The self-assembly of the systems during the hydrothermal process proceeds via the participation of these functional groups. However, graphene is readily re-staked during the hydrothermal process. This reduces the efficient surface area of the carbon support [23]. Therefore, compared with the two-dimensional (2D) networks, the 3D structured graphene is more efficient for ORR as it contains porous structures and functions through multiple electron and mass transfer pathways, which can not only help avoid the re-stacking of graphene layers but also protect the Fe_3O_4 nanoparticles from agglomeration and corrosion. The choice of iron and nitrogen sources is the key to synthesizing Fe_3O_4 nanoparticles-decorated 3D structured graphene composite catalysts. He et al. [24] combined Fe^{3+} and GO via the electrostatic forces to synthesize the precursor of the Fe_3O_4/rGO composite, while Yin et al. [23] synthesized the composite catalyst by exploiting the π–π interactions between iron (II) phthalocyanine and GO suspension. However, the weak binding force observed in electrostatic forces, and the high cost of iron (II) phthalocyanine make it necessary to find a more suitable raw material. As an extremely easy-to-synthesize complex, Fe(II) phenanthroline complex ($[Fe(phen)_3]^{2+}$) can combine with GO through both electrostatic forces and

−π interactions. This complex has never been used as the Fe and N sources to prepare Fe_3O_4/graphene composite catalysts for ORR.

Hence, we synthesized a 3D Fe_3O_4-decorated nitrogen-doped graphene aerogel (Fe_3O_4/NGA) as a highly durable electrocatalyst for ORR via the hydrothermal self-assembly of $[Fe(phen)_3]^{2+}$ and GO. The process was followed by the process of annealing in N_2. As sources of iron and nitrogen, $[Fe(phen)_3]^{2+}$ could be attached with GO via the oxygen-containing groups. The conjugated structure of phenanthroline makes it feasible to attach to graphene via π−π interactions to form a stable suspension in the absence of an additional chemical stabilizer. The interactions between $[Fe(phen)_3]^{2+}$ and GO can not only prevent the re-staking of the graphene layers during the hydrothermal process but also helps avoid severe agglomeration of Fe_3O_4 nanoparticles during the process of annealing treatment. The Fe_3O_4/NGA composite electrocatalyst exhibited a good catalytic activity, with the half-wave potential being 0.81 V and the onset potential being 1.02 V at 0.1 mA cm^{-2}. In addition, the Fe_3O_4/NGA exhibited excellent methanol tolerance and stability, as well as the high selectivity with low H_2O_2 yield (<5%).

2. Experimental Section

2.1 Synthesis of Fe_3O_4/NGA

GO (100 mg) was prepared following a modified Hummer's method. Subsequently, it was dispersed in 40 mL of deionized water to form a homogeneous suspension under conditions of ultrasonication. The mixture was continuously stirred. Following this, the solution containing $[Fe(phen)_3]^{2+}$ (100 mg), which was prepared by dissolving $Fe(Ac)_2$ and phenanthroline (phen) in the molar ratio of 1:3 in 10 mL deionized water, was added dropwise to the GO suspension under conditions of stirring. The process was continued for 3 h. Subsequently, the mixed suspension was transferred to a 100 mL Teflon-lined autoclave and reacted at 180°C for 12 h. Finally, the as-prepared cylindrical gel was freeze-dried overnight and annealed in an atmosphere of N_2 at 900°C for 2 h. The heating rate was maintained at 5°C min^{-1} to prepare the composite catalyst Fe_3O_4/NGA-1.0-900. The contrast catalysts were prepared following the same procedure described above. The conditions of addition of $[Fe(phen)_3]^{2+}$ and the annealing temperature were changed, and the final product was labeled Fe_3O_4/NGA-R-T (R represents the mass ratio between $[Fe(phen)_3]^{2+}$ and GO, and T represents the annealing temperature).

2.2 Characterization

Scanning electron microscopy (SEM, Quanta 250FEG), transmission electron microscopy (TEM, JEOL JEM-2100F), high-resolution TEM (HRTEM), and energy-dispersive X-ray spectroscopy (EDS mapping) techniques were used to analyze the morphology of the catalysts. In addition, X-ray diffraction (XRD) patterns were recorded on a Bruker D8 Advance system (Cu Kα radiation, λ = 1.5408 Å). Raman spectra were recorded on a LabRam Aramis using a 532 nm laser. The X-ray photoelectron spectroscopy (XPS) technique was used for sample analysis (ESCALAB 250; monochromic Al X-ray source). The Brunauer-Emmett-Teller (BET) data were recorded on Micromeritics ASAP 2460.

2.3 Electrochemical Measurements

The electrochemical measurements were carried out on an RRDE-3A Rotating Ring Disk Electrode Rotator Ver.1.2 using a three-electrode system. A rotating disk electrode (RDE, Φ 3 mm), a graphite rod, and an Ag/AgCl (saturated KCl) system were used as the working, counter, and reference electrodes, respectively. The catalyst (5 mg) was dispersed in 1 mL of an aqueous solution (50 µL; 5 wt.% Nafion + 200 µL ethanol + 750 µL DI water) by ultrasonication over a period of 1 h. Following this, 5 µL of the ink was dropped onto the surface of the RDE. The mass loading of the catalyst was 353 µg cm^{-2}.

The cyclic voltammetry (CV) technique was used for sample analysis. An N_2-saturated and O_2-saturated 0.1 M KOH solution was used to record the data at a scan rate of 10 mV s^{-1}. The linear sweep voltammetry (LSV) method was used for analysis using an O_2-saturated 0.1 M KOH solution by varying the rotating rates (400, 625, 900, 1225, 1600, and 2025 rpm at 10 mV s^{-1}). The obtained potential values were converted to the *vs.* RHE scale using the Nernst equation: $E_{RHE} = E_{Ag/AgCl} + 0.0591\mathrm{pH} + 0.197$. The number of transferred electrons (*n*) was calculated using the following Koutecký-Levich (K-L) equation:

$$1/j = 1/j_k + 1/j_d = 1/j_k + 1/\left(B\omega^{\frac{1}{2}}\right), \quad (1)$$

$$B = 0.62nFD_{O_2}^{\frac{2}{3}}\upsilon^{-\frac{1}{6}}C_{O_2}, \quad (2)$$

where *j* is the disk current density; j_k is the kinetic current density, j_d is the diffusion-limiting current density; *B* is the Levich constant, *ω* is the rotating rate, *F* (96485 C mol^{-1}) is the Faradic constant, D_{O2} (1.86 × 10^{-5} cm^2 s^{-1}) is the diffusion coefficient of O_2, *υ* (0.01 cm^2 s^{-1}) is the kinematic viscosity of the electrolyte, and C_{O2} (1.21 × 10^{-6} mol cm^{-3}) is the O_2 concentration in the electrolyte.

The rotating ring disk electrode (RRDE) measurement technique was used to test the productive rate of HO_2^- (%HO_2^-) and determine the value of n in O_2-saturated 0.1 M KOH. The rotating rate was maintained at 1600 rpm at 10 mV s^{-1}. The potential of the Pt ring was set at 1.5 V *vs.* RHE. The values of %HO_2^- and n were calculated as follows:

$$\%HO_2^- = 200 \times \frac{\frac{I_r}{N}}{I_d + \frac{I_r}{N}}, \quad (3)$$

$$n = 4 \times \frac{I_d}{I_d + \frac{I_r}{N}}, \quad (4)$$

where I_r is the ring current, I_d is the disk current, and *N* is the current collection efficiency of the Pt ring, which was determined to be 0.424.

Methanol resistance was measured by current-time (i-t) chronoamperometry in O_2-saturated 0.1 M KOH at a rotating speed of 1600 rpm at the potential of -0.3 V (*vs.* Ag/AgCl), where 2M CH_3OH was added into the electrolyte at approximately 180 s. The long-term stability was characterized by

comparing the polarization curves before and after 10000 CV cycles and the i-t curve at the potential of -0.3 V (*vs.* Ag/AgCl) at 1600 rpm.

3. Results and Discussion

The Fe_3O_4/NGA composite catalyst was synthesized following a simple hydrothermal method and a subsequent annealing process, as illustrated in Figure 1. The detailed synthetic process is described in the experimental section in supporting information. The XRD patterns presented in Figure 2a and Figure 2b reveal the crystalline phases of the catalysts formed under conditions of different ratios and temperatures. The peak at 26° corresponds to the (002) plane of graphite carbon. As shown in Figure 2a, the intensity of the diffraction peaks corresponding to Fe_3O_4 (PDF #16-0629) increases with an increase in the annealing temperature, indicating that 900°C is the suitable annealing temperature to obtain the crystalline Fe_3O_4 phase. We also investigated the effect of the amount of the complex $[Fe(phen)_3]^{2+}$ on the final product, as shown in Figure 2b. Initially, it was believed that 1:1 is the suitable mass ratio between the $[Fe(phen)_3]^{2+}$ complex and GO. In addition, the graphitization degrees of graphene were characterized by analyzing the Raman spectra, in which the D-band at 1360 cm^{-1} and G-band at 1590 cm^{-1} represent the disordered carbon and graphitic carbon, respectively. As shown in Figure 2c and Figure 2d, the catalysts prepared under the same addition conditions of the $[Fe(phen)_3]^{2+}$ complex but at different annealing temperatures (Fe_3O_4/NGA-1.0-700/800/900) exhibit a similar intensity ratio for the D and G-bands (I_D/I_G). However, the I_D/I_G values of the samples prepared under the same pyrolyzing temperature (Fe_3O_4/NGA-0.5/1.0/1.5-900) increase significantly as the amount of the $[Fe(phen)_3]^{2+}$ complex increases, indicating that the content of the $[Fe(phen)_3]^{2+}$ complex and not the annealing temperature primarily influences the defective degree of graphene. This can indirectly explain the doping level of graphene [25].

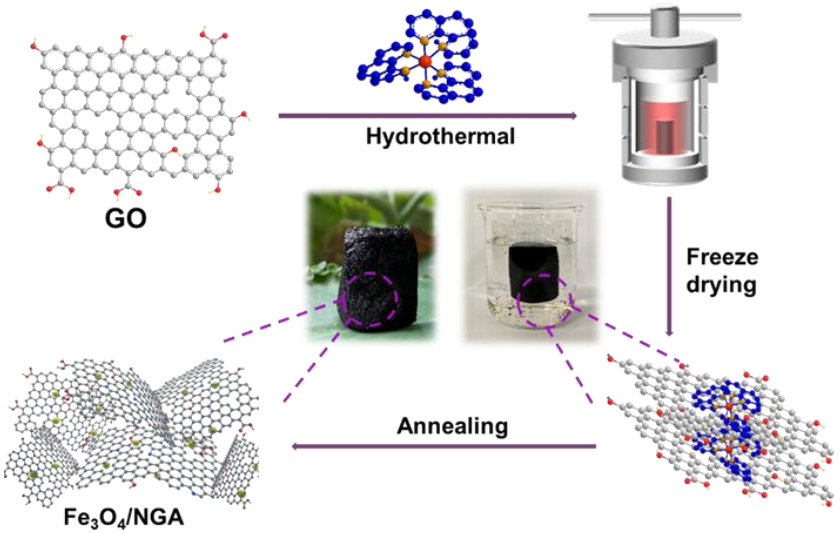

Figure 1 Schematic illustration of the synthesis process of Fe_3O_4/NGA.

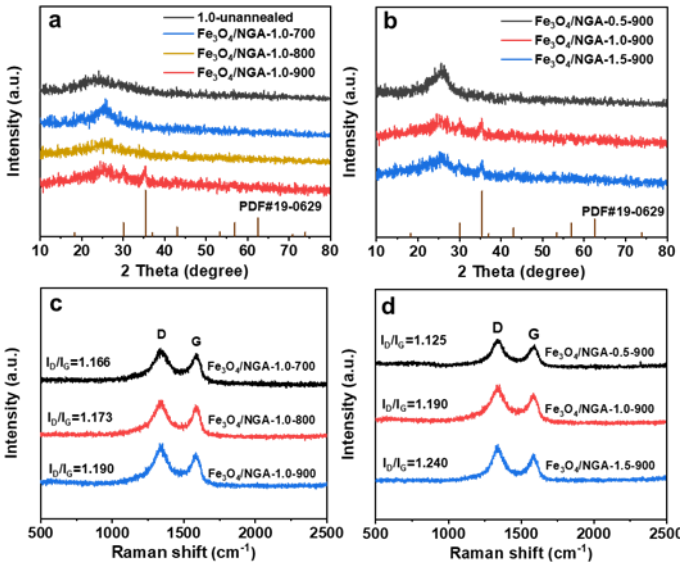

Figure 2 X-ray diffraction (XRD) patterns recorded for Fe_3O_4/NGA under conditions of (a) varying annealing temperatures and (b) varying $[Fe(phen)_3]^{2+}$ contents. Raman spectra of Fe_3O_4/NGA recorded under conditions of (c) varying annealing temperatures and (d) varying $[Fe(phen)_3]^{2+}$ conditions.

The morphology and structure of Fe_3O_4/NGA-1.0-900 are characterized using the SEM technique, as shown in Figures 3a-c. As shown in Figure 3a and Figure 3b, the graphene units present an interconnected network with a porous structure. The results of BET analysis are presented in Figure S1, and the results reveal that Fe_3O_4/NGA-1.0-900 presents a type IV isotherm because of the presence of a hysteresis loop at high partial pressures. This indicates the presence of a mesoporous structure [26, 27]. The Barret-Joyner-Halenda (BJH) pore size distribution presented in Figure S1b shows that a large proportion of the mesopores lies in the range of 10-50 nm for the Fe_3O_4/NGA-1.0-900 sample. The SEM-EDS mapping images presented in Figure 3c demonstrate that the Fe, N, C, and O elements are homogeneously distributed in the Fe_3O_4/NGA-1.0-900 catalyst. The composition and crystalline structure are further illustrated using the TEM and HRTEM characterization techniques, as shown in Figures 3d-g. Analysis of Figure 3d and Figure 3e reveals that the Fe_3O_4 nanoparticles in size range of 10-60 nm are homogenously anchored to the graphene network. The HRTEM images were analyzed, and the interplanar spacings of 0.242 and 0.290 nm corresponded to the (222) and (220) lattice planes of the Fe_3O_4 phase (PDF #16-0629). This further indicates the successful synthesis of the Fe_3O_4 crystal.

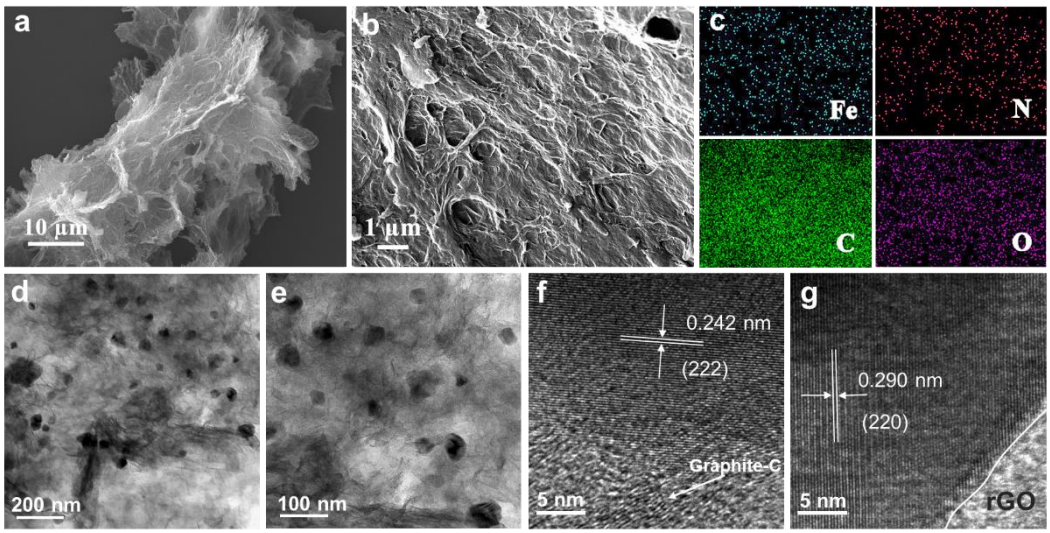

Figure 3 (a, b) Scanning electron microscopy (SEM), (c) energy-dispersive X-ray spectroscopy (EDS) mapping, (d, e) transmission electron microscopy (TEM), and (f, g) high-resolution TEM (HRTEM) images of Fe_3O_4/NGA-1.0-900.

The XPS technique was used to analyze the chemical composition of the Fe_3O_4/NGA-1.0-900 catalyst. Figure 4a shows the high-resolution XPS spectrum of C 1s, and the peaks at 284.8, 286.0, 287.3, and 288.8 eV correspond to the sp^2 carbon C =C, C-O, C-N, and O-C =O groups, respectively [24, 28]. The spectrum of N 1s in Figure 4b can be fitted into four peaks that correspond to the pyridinic-N (398.5 eV), Fe-N (399.4 eV), pyrrolic-N (400.8 eV), and graphitic-N (401.8 eV) units. The N species (N doped carbon), especially pyridinic-N and Fe-N, facilitate the process of ORR [29, 30]. In addition, the presence of Fe-N demonstrates the interaction between the Fe_3O_4 nanoparticles and the N-doped graphene. In the spectrum of Fe 2p in Figure 4c, there are two characteristic peaks at 711.45 and 724.8 eV corresponding to the Fe $2p_{3/2}$ and Fe $2p_{1/2}$ units of Fe_3O_4, respectively [31, 32]. The absence of satellite peaks demonstrates that the Fe species is present as Fe_3O_4 in the catalyst [14, 24, 32]. The O 1s spectrum (Figure 4d) can be divided into three peaks appearing at the binding energies of 530.5 (Fe-O), 532.1 (O-C =O), and 533.56 eV (C-OH) [33]. The analysis of the XPS profiles demonstrates the presence of Fe_3O_4 and the successful doping of N into graphene.

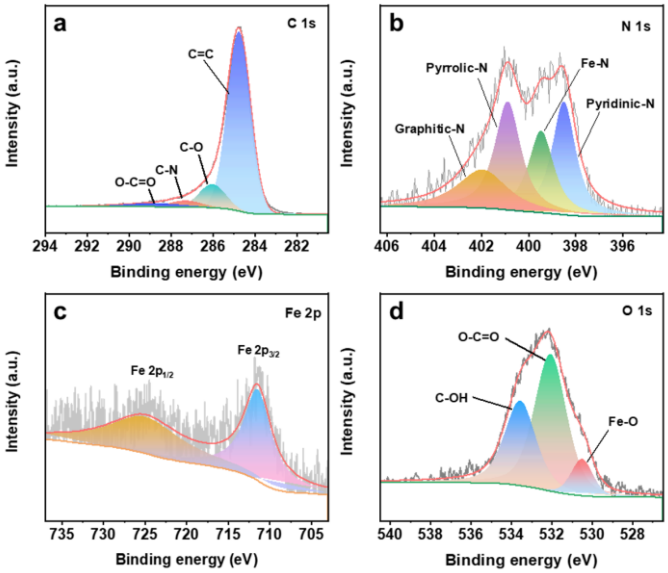

Figure 4 High-resolution X-ray photoelectron spectroscopy (XPS) spectral profiles of (a) C 1s, (b) N 1s, (c) Fe 2p, and (d) O 1s in Fe_3O_4/NGA-1.0-900.

The electrochemical performance of the Fe_3O_4/NGA-1.0-900 system and other contrast catalysts was performed using a three-electrode system. First, to evaluate the electrocatalytic activity of Fe_3O_4/NGA-1.0-900 towards ORR, the cyclic voltammetry (CV) technique was used for analysis in N_2 and O_2-saturated 0.1 M KOH electrolyte. As shown in Figure S2, a significantly intense reduction peak is observed in the CV curve recorded for Fe_3O_4/NGA-1.0-900 in an O_2-saturated 0.1 M KOH solution. Cathodic peaks did not appear in the curves recorded in N_2-saturated 0.1 M KOH, demonstrating that the Fe_3O_4/NGA-1.0-900 catalyst exhibits electrocatalytic activity for ORR. To further investigate the electrocatalytic performance, the linear sweep voltammetry (LSV) method was used in O_2-saturated 0.1 M KOH electrolyte at a rotating rate of 1600 rpm at 10 mV s^{-1}. As shown in Figure 5a and Figure 5b, the LSV curves of the Fe_3O_4/NGA catalysts synthesized at varying ratios and temperatures exhibit significantly different electrocatalytic activities. The Fe_3O_4/NGA-1.0-900 catalyst shows a half-wave potential ($E_{1/2}$) of 0.81 V *vs.* RHE, and an onset potential (E_{onset}) of 1.02 V *vs.* RHE at 0.1 mA cm^{-2}, which are closer to the values recorded for the Pt/C catalyst ($E_{1/2}$ = 0.83 V *vs.* RHE, E_{onset} = 1.00 V *vs.* RHE). As the annealing temperature increases, the half-wave potential becomes more positive, indicating the enhanced catalytic activity for ORR. These results, combined with the results obtained by analyzing the XRD patterns recorded for the Fe_3O_4/NGA-1.0-700/800/900 catalysts, reveal that the crystalline degree of the Fe_3O_4 nanoparticles is positively related to the electrocatalytic activity of the composite catalyst Fe_3O_4/NGA. In addition, the difference in the electrocatalytic activities of the samples prepared under conditions of varying contents of $[Fe(phen)_3]^{2+}$ complex is more pronounced than that of the catalysts prepared under conditions of varying pyrolysis temperatures. This indicates that the quantity of the Fe_3O_4 nanocrystals has a significant influence on the electrocatalytic activity of the composite catalyst. In addition, the electrochemical active surface area (ECSA) is also an important factor in evaluating the performance of the electrocatalysts. As shown in Figures S3a-e, the ECSA of the catalysts was assayed as the double-layer capacitance (C_{dl}), which was calculated by analyzing the CV curves recorded at different scan rates in the potential range in the absence of redox processes (1.065-1.165 V *vs.* RHE). In Figure S3f, the Fe_3O_4/NGA-1.0-900 catalyst presents the maximum C_{dl} of 21.48

mF cm^{-2}, indicating the maximum ECSA among these catalysts. The Fe_3O_4/NGA-1.0-900 system exhibits the best electrocatalytic activity for ORR among these catalysts, and this can be attributed to the improvement in the ECSA values.

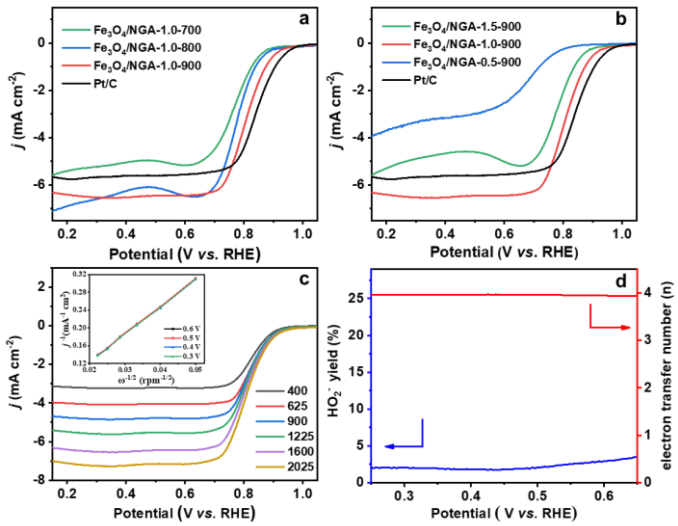

Figure 5 Linear sweep voltammetry (LSV) curves recorded for Fe_3O_4/NGA under conditions of (a) varying annealing temperatures and at (b) different addition amounts of $[Fe(phen)_3]^{2+}$ (rotating rate: 1600 rpm). (c) LSV curves recorded for Fe_3O_4/NGA-1.0-900 at different rotating rates, and the corresponding K-L plots are presented in the inset. (d) HO_2^- yield and the electron transferred number for Fe_3O_4/NGA-1.0-900. The experiments were conducted in O_2-saturated 0.1 M KOH electrolytes at the scan rate of 10 mV s^{-1}.

To understand the catalytic mechanism associated with ORR carried out with the Fe_3O_4/NGA-1.0-900 composite catalyst, the RDE and RRDE methods were used, as shown in Figure 5c and Figure 5d. As one can see from the inset in Figure 5c, the corresponding K-L plots obtained at different potential values show good parallelism and linearity with the calculated electron transferred number of ~4.0 at 0.3, 0.4, 0.5, and 0.6 V *vs.* RHE, indicating that the ORR process proceeds in this system following a four-electron transfer pathway. In addition, the results of RRDE measurements in Figure 5d reveal that the yield of HO_2^- is less than 5%, and the electron transfer number is close to 4. This indicates the high catalytic selectivity of Fe_3O_4/NGA-1.0-900. Besides the catalytic activity, the long-time stability and methanol tolerance are also important characteristics of electrocatalysts. As shown in Figure 6a, following the injection of methanol at 180 s, the current density corresponding to the Fe_3O_4/NGA-1.0-900 catalyst remains almost unchanged, while that of the Pt/C catalyst decreases significantly. This illustrates the excellent methanol resistance of Fe_3O_4/NGA-1.0-900. The long-term stability was initially studied by comparing the initial LSV curve and the curve recorded after 10000 CV cycles. As shown in Figure 6b, the variation in the LSV polarization curves recorded for the Fe_3O_4/NGA-1.0-900 system is negligible, while the LSV curve recorded for the Pt/C shifts negatively after 10000 CV cycles. In addition, the i-t chronoamperometry test was also carried out at -0.3 V *vs.* Ag/AgCl for 20000 s to evaluate the stability of the electrocatalyst, as shown in Figure 6c. Compared with the Pt/C catalyst, the Fe_3O_4/NGA-1.0-900 composite catalyst displays a better long-time performance ability, with the current retention value being 89.13%. In brief, the

Fe_3O_4/NGA-1.0-900 composite catalyst exhibits excellent stability in terms of long-time durability and methanol tolerance.

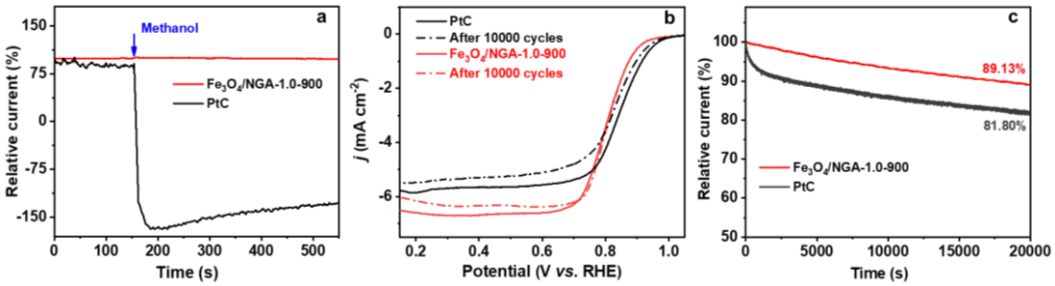

Figure 6 (a) Methanol tolerance, (b, c) long-time durability of Fe_3O_4/NGA-1.0-900. The experiments were conducted in O_2-saturated 0.1 M KOH electrolyte at a rotating speed of 1600 rpm at 10 mV s^{-1}.

To verify the relationship between the composite catalyst and electrocatalytic performance, the Fe_3O_4/NGA-1.0-900 system was etched in 1 M HCl for 12 h to remove the Fe_3O_4 species. As shown in Figure S4a, the characteristic peaks of Fe_3O_4 disappear following acid etching. Compared with Fe_3O_4/NGA-1.0-900, the catalytic performance deteriorates significantly post acid etching. This verifies that the Fe_3O_4 nanoparticles are the dominant active sites in the Fe_3O_4/NGA-1.0-900 composite catalyst. The result is consistent with the results obtained by analyzing the XRD patterns and electrochemical performance. The crystallinity of Fe_3O_4 increases with an increase in the annealing temperature (Figure 2a). Meanwhile, the electrocatalytic activity of the electrocatalyst for ORR increases with an increase in the annealing temperature. This also indicates the dominance of the Fe_3O_4 nanoparticles in the composite catalyst. In addition, as revealed by the LSV curves presented in Figure S4b, the catalyst produced after acid etching retains part of catalytic activity. The half-wave potential recorded under these conditions was 0.72 V *vs.* RHE, indicating that the N-doped graphene unit also contributes to the catalytic activity of the composite catalyst. As shown in the Raman spectral profile in Figure 2c, the degree of disorder of carbon increases as the annealing temperature increases. This also contributes to the high electrocatalytic activity of Fe_3O_4/NGA-1.0-900. In short, the electrocatalytic performance of the Fe_3O_4/NGA-1.0-900 composite catalyst for ORR can be primarily attributed to the highly crystalline Fe_3O_4 nanoparticles.

4. Conclusions

A 3D Fe_3O_4-decorated nitrogen-doped graphene aerogel (Fe_3O_4/NGA) electrocatalyst was successfully synthesized via the hydrothermal self-assembly of the Fe(II)phenanthroline complex ($[Fe(phen)_3]^{2+}$) and GO. The process was followed by an annealing process in an atmosphere of N_2. The Fe_3O_4/NGA-1.0-900 catalyst with the suitable experimental variable exhibits excellent activity, and the half-wave potential was recorded to be 0.81 V *vs.* RHE. Excellent long-term durability and methanol tolerance were also recorded. The results demonstrate that the Fe_3O_4 nanoparticles and N-doped graphene aerogel can be used to effectively improve the catalytic activity in the cases of ORR. The increase in activity can be attributed to the dominant active sites of the Fe_3O_4 nanocrystalline systems. The results reveal that the Fe_3O_4/NGA composite catalyst is a promising candidate that can be used for the fabrication of non-precious electrocatalysts for ORR.

Author Contributions

Jia Yu is the first author in this paper, her contrubutions include experimental design and operation, electrochemical measurements, and the writing of the paper. Haiyan Jing, Zudeng Wu, and Boyuan Liu are the authors who help to operate the characterazation equipment.

Funding

The work was supported by the National Natural Science Foundation of China (Nos. 51972173, 51872140), the program for Science and Technology Innovative Research Team in Universities of Jiangsu Province, Jiangsu Key Laboratory of Advanced Catalytic Materials and Technology (BM2012110), and '333 program' (BRA2019262) of Jiangsu Province, China.

Competing Interests

The authors have declared that no competing interests exist.

Additional Materials

The following additional materials are uploaded at the page of this paper.

1. Figure S1: (a) N_2 adsorption–desorption isotherm, and (b) Barret-Joyner-Halenda (BJH) pore size distribution of Fe_3O_4/NGA-1.0-900.
2. Figure S2: Cyclic voltammetry (CV) curves recorded for Fe_3O_4/NGA-1.0-900 in N_2 and O_2-saturated 0.1 M KOH at a scan rate of 50 mV s^{-1}.
3. Figure S3: CV curves recorded for (a) Fe_3O_4/NGA-1.0-700, (b) Fe_3O_4/NGA-1.0-800, (c) Fe_3O_4/NGA-1.0-900, (d) Fe_3O_4/NGA-1.5-900, and (e) Fe_3O_4/NGA-0.5-900 at the scan rates of 10, 20, 30, 40, and 50 mV s^{-1}. (f) Current densities (recorded at the potential of 1.115 V) as a function of the scan rate derived from (a)–(e).
4. Figure S4: (a) X-ray diffraction (XRD) patterns and (b) Linear sweep voltammetry (LSV) curves recorded for Fe_3O_4/NGA-1.0-900 before and after acid etching.
5. Abbreviation list.
6. Table S1: Comparison of the electrochemical ORR performances of Fe3O4/NGA-1.0-900 recorded with the representative transition-metal-based catalysts (electrolyte is 0.1 M KOH).

References

1. Tang K, Hu H, Xiong Y, Chen L, Zhang J, Yuan C, et al. Hydrophobization engineering of the air-cathode catalyst for improved oxygen diffusion towards efficient zinc-air batteries. Angew Chem Int Ed. 2022; 61: e202202671.
2. Cui J, Q Chen, X Li, S Zhang. Recent advances in non-precious metal electrocatalysts for oxygen reduction in acidic media and PEMFCs: An activity, stability and mechanism study. Green Chem. 2021; 23: 6898-6925.
3. Zhou Z, Kong Y, Tan H, Huang Q, Wang C, Pei Z, et al. Cation-vacancy-enriched nickel phosphide for efficient electrosynthesis of hydrogen peroxides. Adv Mater. 2022; 34: 2106541.

4. Reshetenko T, Odgaard M, Randolf G, Ohtaki KK, Bradley JP, Zulevi B, et al. Design of PGM-free cathodic catalyst layers for advanced PEM fuel cells. Appl Catal B. 2022; 312: 121424.
5. Askari MB, Rozati SM, Di Bartolomeo A. Fabrication of Mn_3O_4-CeO_2-rGO as nanocatalyst for electro-oxidation of methanol. Nanomaterials. 2022; 12: 1187.
6. Askari MB, Salarizadeh P, Seifi M, Ramezan zadeh MH, Di Bartolomeo A. $ZnFe_2O_4$ nanorods on reduced graphene oxide as advanced supercapacitor electrodes. J Alloys Compd. 2021; 860: 158497.
7. Askari MB, Salarizadeh P, Di Bartolomeo A. $NiCo_2O_4$-rGO/Pt as a robust nanocatalyst for sorbitol electrooxidation. Int J Energy Res. 2022; 46: 6745-6754.
8. Dong Q, Mo Z, Wang H, Ji S, Wang X, Linkov V, et al. N-doped carbon networks containing inserted FeNx@NC nanospheroids and bridged by carbon nanotubes as enhanced catalysts for the oxygen reduction reaction. ACS Sustain Chem Eng. 2020; 8: 6979-6989.
9. Li T, Li M, Zhang M, Li X, Liu K, Zhang M, et al. Immobilization of Fe_3N nanoparticles within N-doped carbon nanosheet frameworks as a high-efficiency electrocatalyst for oxygen reduction reaction in Zn-air batteries. Carbon. 2019; 153: 364-371.
10. Wang Q, Lei Y, Chen Z, Wu N, Wang Y, Wang B, et al. Fe/Fe_3C@C nanoparticles encapsulated in N-doped graphene-CNTs framework as an efficient bifunctional oxygen electrocatalyst for robust rechargeable Zn-air batteries. J Mater Chem A. 2018; 6: 516-526.
11. Marghaki NS, Jonoush ZA, Rezaee A. Chromium (VI) removal using microbial cellulose/ nano-Fe_3O_4 @polypyrrole: Isotherm, kinetic and thermodynamic studies. Mater Chem Front. 2022; 278: 125696.
12. Jonoush ZA, Rezaee A, Ghaffarinejad A. Enhanced electrocatalytic denitrification using non-noble Ni-Fe electrode supplied by Fe_3O_4 nanoparticle and humic acid. Appl Surf Sci. 2021; 563: 150142.
13. Marghaki NS, Jonoush ZA, Rezaee A. Improving the performance of Cr (VI) removal by electrochemical process using microbial cellulose/magnetic nanoparticles electrode. J Clean Prod. 2020; 277: 123195.
14. Liu Y, Qiao B, Jia N, Shi S, Chen X, An Z, et al. Efficient bifunctional oxygen electrocatalysts for rechargeable zinc–air battery: Fe3O4/N−C nanoflowers derived from aromatic polyamide. ChemCatChem. 2022; 4: e202101523.
15. Wang H, Wang W, Xu YY, Dong S, Xiao J, Wang F, et al. Hollow nitrogen-doped carbon spheres with Fe_3O_4 nanoparticles encapsulated as a highly active oxygen-reduction catalyst. ACS Appl Mater Interfaces. 2017; 9: 10610-10617.
16. Yan L, Wang H, Shen J, Ning J, Zhong Y, Hu Y. Formation of mesoporous Co/CoS/Metal-N-C@S, N-codoped hairy carbon polyhedrons as an efficient trifunctional electrocatalyst for Zn-air batteries and water splitting. Chem Eng J. 2021; 403: 126385.
17. Zhu C, Yang W, Di J, Zeng S, Qiao J, Wang X, et al. CoNi nanoparticles anchored inside carbon nanotube networks by transient heating: Low loading and high activity for oxygen reduction and evolution. J Energy Chem. 2020; 54: 63-71.
18. Zhong X, Yi W, Qu Y, Zhang L, Bai H, Zhu Y, et al. Co single-atom anchored on Co_3O_4 and nitrogen-doped active carbon toward bifunctional catalyst for zinc-air batteries. Appl Catal B. 2020; 260: 118188.

19. Zhang X, Han X, Jiang Z, Xu J, Chen L, Xue Y, et al. Atomically dispersed hierarchically ordered porous Fe–N–C electrocatalyst for high performance electrocatalytic oxygen reduction in Zn-Air battery. Nano Energy. 2020; 71: 104547.
20. Yang H, Shang L, Zhang Q, Shi R, Waterhouse GIN, Gu L, et al. A universal ligand mediated method for large scale synthesis of transition metal single atom catalysts. Nat Commun. 2019; 10: 4585.
21. Lim J, Jung JW, Kim NY, Lee GY, Lee HJ, Lee Y, et al. N_2-dopant of graphene with electrochemically switchable bifunctional ORR/OER catalysis for Zn-air battery. Energy Stor Mater. 2020; 32: 517-524.
22. Xiang Q, Liu Y, Zou X, Hu B, Qiang Y, Yu D, et al. Hydrothermal synthesis of a new kind of N-doped graphene gel-like hybrid as an enhanced ORR electrocatalyst. ACS Appl Mater Interfaces. 2018; 10: 10842-10850.
23. Yin H, Zhang C, Liu F, Hou Y. Hybrid of iron nitride and nitrogen-doped graphene aerogel as synergistic catalyst for oxygen reduction reaction. Adv Funct Mater. 2014; 24: 2930-2937
24. He X, Long X, Wang P, Wu H, Han P, Tang Y, et al. Interconnected 3D Fe_3O_4/rGO as highly durable electrocatalyst for oxygen reduction reaction. J Alloys Compd. 2021; 855: 157422.
25. Chen X, Ma DD, Chen B, Zhang K, Zou R, Wu XT, et al. Metal–organic framework-derived mesoporous carbon nanoframes embedded with atomically dispersed Fe–Nx active sites for efficient bifunctional oxygen and carbon dioxide electroreduction. Appl Catal B. 2020; 267: 118720.
26. Wu K, Zhang L, Yuan Y, Zhong L, Chen Z, Chi X, et al. An iron-decorated carbon aerogel for rechargeable flow and flexible Zn-air batteries. Adv Mater. 2020; 32: e2002292.
27. Zhang T, Bian J, Zhu Y, Sun C. FeCo Nanoparticles encapsulated in N-doped carbon nanotubes coupled with layered double (Co, Fe) hydroxide as an efficient bifunctional catalyst for rechargeable zinc-air batteries. Small. 2021; 17: e2103737.
28. Ahmed MS, Begum H, Kim YB. Iron nanoparticles implanted metal-organic-frameworks based Fe–N–C catalysts for high-performance oxygen reduction reaction. J Power Sources. 2020; 451: 227733.
29. Gao S, Fan B, Feng R, Ye C, Wei X, Liu J, et al. N-doped-carbon-coated Fe_3O_4 from metal-organic framework as efficient electrocatalyst for ORR. Nano Energy. 2017; 40: 462-470.
30. Lin SY, Xia LX, Cao Y, Meng HL, Zhang L, Feng JJ, et al. Electronic regulation of ZnCo dual-atomic active sites entrapped in 1D@2D hierarchical N-doped carbon for efficient synergistic catalysis of oxygen reduction in Zn-air battery. Small. 2022; 18: e2107141.
31. Wang Y, Wu M, Wang K, Chen J, Yu T, Song S. Fe_3O_4@N-doped interconnected hierarchical porous carbon and its 3D integrated electrode for oxygen reduction in acidic media. Adv Sci. 2020; 7: 2000407.
32. Wu Q, Yu R, Zhou Z, Liu H, Jiang R. Encapsulation of a core-shell porous Fe_3O_4@carbon material with reduced graphene oxide for Li(+) battery anodes with long cyclability. Langmuir. 2021; 37: 785-792.
33. Hao R, Chen J, Wang Z, Zhang J, Gan Q, Wang Y, et al. Iron polyphthalocyanine-derived ternary-balanced Fe_3O_4/Fe_3N/Fe-N-C@PC as a high-performance electrocatalyst for the oxygen reduction reaction. Sci China Mater. 2021; 64: 2981-2996.

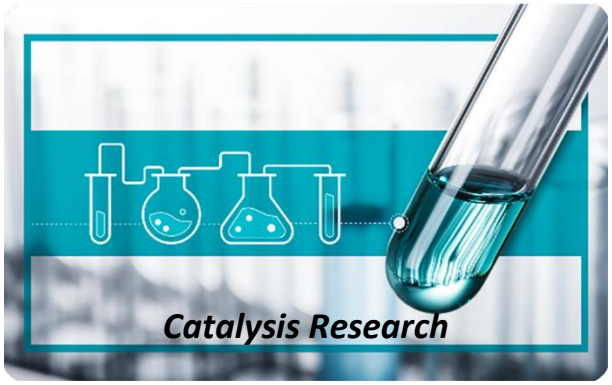

Enjoy *Catalysis Research* by:

1. Submitting a manuscript
2. Joining in volunteer reviewer bank
3. Joining Editorial Board
4. Guest editing a special issue

For more details, please visit:
http://www.lidsen.com/journals/cr